Polarimetry with disordered photonic structures

Michael Juhl[*,†] and Kristjan Leosson[†,‡]

†Innovation Center Iceland, Arleynir 2-8, Reykjavik Iceland

‡Science Institute, University of Iceland, Dunhagi 5, Reykjavik, Iceland

E-mail: michaeljuhl@nmi.is

Phone: +354 5229000

Abstract

In conventional Stokes polarimetry, where the polarimetric information is obtained from a series of intensity measurements, stable and accurate measurements typically require the optical elements to be carefully designed. Here, we propose a paradigm shift where deep neural network assisted polarimeters based on disordered photonic structures perform high quality polarimetric measurements while completely removing the need for specially designed polarization analyzers, demonstrating how disordered photonic structures fabricated without the use of any nanolithography techniques can enable accurate analysis of optical signals. We implement this concept with disorder-engineered nano-scatterers that allow for analyzing varying degrees of disorder and cellophane film that demonstrate the cost-saving potential of the concept. We demonstrate polarimetric performances, calibrated using deep neural networks, that are comparable to commercial polarimeters, does not require prior knowledge of the input wavelength and show a high degree of mechanical stability.

Keywords

Polarimetry, Polarization-selective devices, Nanophotonics, Disordered photonics, Speckle, Deep neural networks, Machine learning

Introduction

Polarization is an inherent property of electromagnetic waves describing the geometric orientational degrees of freedom of electric field oscillations. Polarimetric measurements provide essential information about the emitting sources and light-matter interactions and are therefore useful in many applications including optical communication, remote sensing, and medical diagnostics. A conventional Stokes polarimeter uses intensity measurements to calculate the four elements in the Stokes vector.[1] The Stokes vector contains information about the state-of-polarization (SOP) as well as the degree-of-polarization (DOP) of the electric field. The SOP and DOP can be visualized as a point on or within a unit sphere (Poincaré sphere). The classical rotating waveplate polarimeter, invented in the mid-nineteenth century,[2] consists of a rotatable quarter-wave plate followed by a linear polarizer and is still an active area of research[3,4] alongside new methods such as fiber based polarimeters,[5] liquid-crystal-based polarimeters[6] and polarimeters based on photoelastic modulators.[7] Recent advances in nanotechnology have enabled new ways of miniaturizing polarimeters with advantages such as simplicity, robustness, cost efficiency and on-chip integration.[8–11] Recently, it has been suggested to use random nanostructures for realization of on-chip polarimetry.[12] Typically, in conventional polarimetry the optical elements that manipulate the polarization for intensity measurements are tailored for specific polarizations to maximize the quality of the measurement. This is also the case in metasurface polarimetry where the polarization analyzer typically consists of carefully designed 2-dimensional nanostructures repeated in periodic or pseudo-periodic grids,[13–16] requiring highly specialized nanofabrication methods. Light scattered in a disordered photonic structure will interfere both during and after the scattering

process thereby scrambling an input signal into a complex interference pattern, or 'speckle pattern'. Despite the seemingly unpredictable output the scattering is predominantly elastic and reversible, and no information is lost in what is actually a deterministic process.[17,18] This has led to a number of interesting applications and devices including lensless focusing and imaging,[19,20] flat lenses,[21,22] increased photovoltaic efficiency,[23] and random lasers.[24,25] Polarimetry based on disordered nanostructures offers the advantages of more relaxed fabrication tolerances compared to the periodic metasurface polarimeters and straightforward achievement of a large amount of polarization analyzer outputs. However, a polarimeter using disordered structures is very sensitive to parameters that change the polarization response, such as wavelength, position and angle of the input light beam.

Machine learning techniques based on deep neural networks, or deep learning, have recently shown great success and potential in many areas of regression and classification problems, mainly due to increases in computing power and easy availability of vast amounts of data.[26] In optics, neural networks have found applications in optical imaging, spectroscopy, optical communication as well as all-optical neural networks.[27–30]

Here we show that signal-saving polarimeters based on structurally disordered nanoantennas or cellophane film, calibrated using a neural network model, produce polarization measurements with a favorable accuracy compared to previously reported metasurface polarimeters as well as commercially available polarimeters. Furthermore, we show that deep learning can be used to increase the robustness of the polarimeter to parameter changes that have an influence on the polarization response. This is realized by incorporating variations in wavelength and position of the input light beam relative to the polarimeter into the neural network model.

Principles and design

Stokes polarimetry requires projective measurements of the content of specific polarization states in the incident light beam. This is performed using a polarization analyzer whose transmitted intensities are proportional to the specific polarization states. In order to obtain the required number of features, the polarization analyzer either splits the measurement in time (time-division) or splits the measurement over space (amplitude-division or wavefront-division). The waveplate polarimeter, which is an example of a time-division polarimeter, typically uses a discrete Fourier transform to obtain the Stokes vector,[31] whereas division-of-intensity polarimetry introduces an analyzer matrix, $\mathbf{A}$, that links the polarization information to measured intensities. Using linear transformation, the Stokes vector $\mathbf{S}$ is reconstructed from the intensity measurements $\mathbf{I}$ of the light manipulated by the analyzer, i.e. $\mathbf{S} = \mathbf{A}^{-1}\mathbf{I}$. The analyzer matrix is obtained from calibration.[32–34] The rows in the analyzer matrix, the analyzer vectors, are proportional to the polarizations investigated by the analyzer. It can be shown that the polarimetric error is minimized when the analyzer vectors are equally spaced on the Poincare sphere.[35] In order to minimize measurement error, the analyzer vector polarizations must therefore be selected carefully, and the physics of the polarization analyzer must be well-controlled (fabrication tolerances must be low). For metasurface polarimeters this means that the size, shape and position of the scattering nanostructures needs to be very precise and control of parameters such as deposition thickness, etch depth, undercut, and/or anisotropy becomes important for the performance of the polarimeter. However, if the number of analyzer vectors are large and the direction of the vectors are randomly distributed over the entire Poincaré sphere, as is the case for a disordered polarization-dependent scattering medium, then it is no longer necessary to carefully design the polarization analyzer. The fabrication of a polarimeter based on a random polarization-dependent medium is therefore potentially much simpler and cheaper than a conventional polarimeter.

We have fabricated polarization-dependent scattering media using gold nanoantennas of

random orientation and quasi-random position. The random metasurfaces were patterned using electron-beam lithography on a transparent material allowing control over the antenna shapes and the degree of randomness. Additionally, a cellophane film has been employed as polarization analyzer to emphasize the simplicity of polarimeters based on disordered materials.

Electron micrographs of nanoantenna patterns are shown in Fig. 1. Fig. 1a–c consists of identical gold nanoantennas with sizes of approximately $250 \times 60 \times 20$ nm. Fullwave simulations of the optical response of individual gold nanorods show localized surface plasmon resonance peaks at around 1550 nm.[36] The antennas are confined within unit cells with a size of two times the antenna length to acheive sufficient intensity of the scattered light. In Fig. 1c each antenna is assigned a random orientation and position within the unit cell, resulting in a polarization analyzer with analyzer vectors distributed randomly across all polarization states. Restricting the antenna orientations to a limited set of angles as in Fig. 1b or a fixed angle as in Fig. 1a will set a constraint on the polarizations selected by the analyzer and will limit the performance of the polarimeter. A design with quasi-randomly positioned gold nanodisks is an alternative approach to nanorods with random orientations (Fig. 1d). In this case changing the shape of the disks from circular to elliptical (see inset) will similarly result in a constraint on the analyzer vectors.

The optical setup, as shown in Fig. 2a, was operated using near-infrared light (1530–1565 nm) from a tunable fiber laser (Tunics-Plus from GN Nettest). The light was directed from a deterministic polarization controller (DPC5500 from Thorlabs) to the polarization analyzer (the sample containing disordered photonic structures) via a mechanically cleaved bare single-mode fiber (SMF-28). The distance between the fiber and the analyzer was 500 µm to achieve a resonable number of speckles received by the camera. The reference polarization of the transmitted light was measured by a commercial waveplate polarimeter (PAN5710IR3 from Thorlabs). The off-axis speckle pattern arising from scattering by the disordered array of nanoantennas or the cellophane film was recorded with a 320×256-pixel InGaAs camera
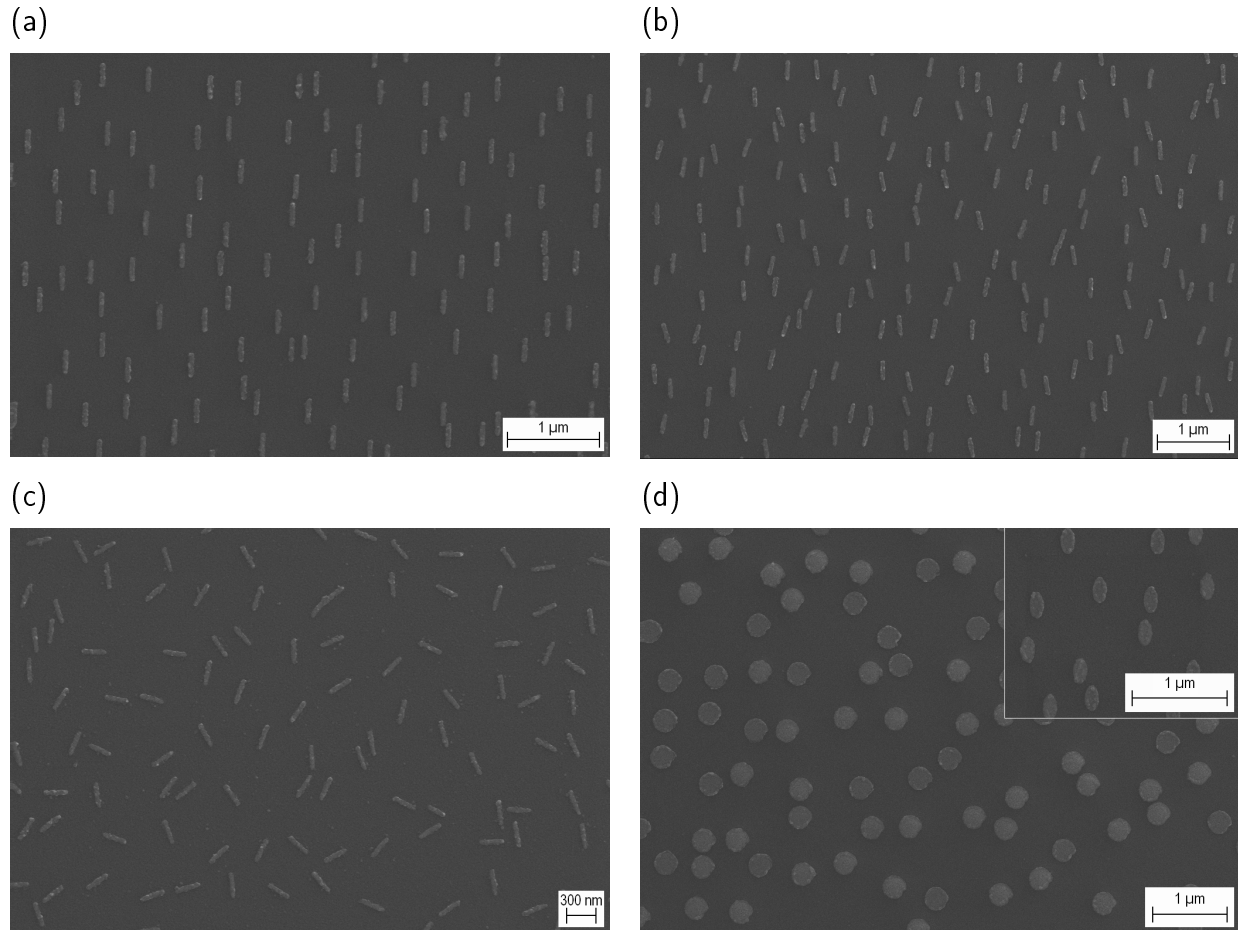
Figure 1: Electron micrograph images of gold nanopatterns. (a)–(c) Gold nanorods with quasi-random positions and (a) fixed vertical orientation, (b) random orientation inside an angular interval of 70°–110°, (c) random orientation. (d) Electron micrograph of circular nanodisks with a radius of approximately 150 nm and a unit cell size of 700 nm. The inset shows a nanostructure of elliptical nanodisks with a = 150 nm and b = 75 nm.

(C10633 from Hamamatsu). A 10X/0.25 optical microscope lens and an extension tube was used to remove background light.

For polarization measurements with the fixed light source position we recorded 120 speckle images at each wavelength step of 0.2 nm. For measurements with variable light source position 240 polarizations were measured at each wavelength step and before each measurement the position of the single-mode fiber was set to a random value within a $20{\times}20{\times}20\,\mu\text{m}$ grid using a piezoelectric motorized xyz stage. The polarization was randomized using the polarization controller's SOP scrambler and the laser power was varied between 1.5 and 3.0 mW. The setup was automated to allow for rapid collection of large data sets required for neural network training with variation of parameters such as polarization, wavelength, laser power, and position of the light beam relative to the sample.

Analytical model

Knowing the position and orientation of each nanoantenna the scattered speckle pattern can be calculated analytically using the dipole approximation. This model does not take into account antenna interactions or fabrication imperfections and it is therefore suited for simulating the general behavior of the speckle pattern although the exact experimental speckle image cannot be predicted.

The far-field radiation pattern of a plasmonic nanoantenna with length less than a wavelength can be modelled reasonably well as a short dipole.[37] The electric field of a short dipole antenna in the far-field is given by

$$\mathbf{E} = i\eta kl\frac{e^{-ikr}}{4\pi r}\mathbf{F}(\theta, \phi)I \tag{1}$$

where $k = 2\pi/\lambda$ is the angular wavenumber, l is the length of the antenna, the characteristic impedance is a function of the permittivity and permeability $\eta = \sqrt{\mu/\varepsilon}$, r is the distance depending on the observation point and θ, ϕ are the corresponding angles. I is the excitation
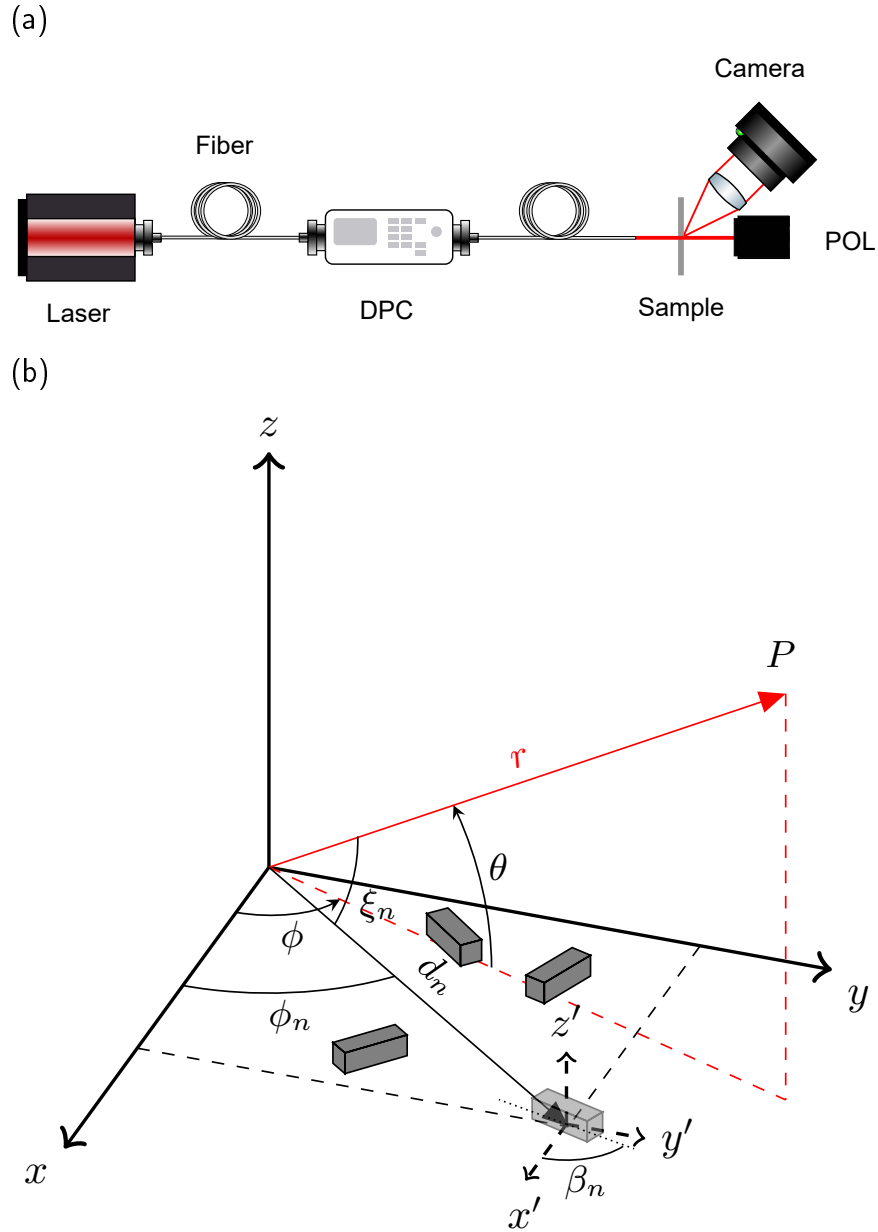
Figure 2: (a) A schematic of the measurement setup showing a fiber laser connected to a deterministic polarization controller (DPC) with a 1550 nm single-mode fiber. A cleaved fiber is aligned to the polarization analyzer (the grey sample) using an xyz stage. A commercial free-space polarimeter (POL) measures the reference polarization and an infrared camera records the scattered speckle pattern. (b) Geometry of an array of nanorod antennas with quasi-random position in the xy plane and arbitrary orientation.

current. The angular-dependent vector $\mathbf{F}(\theta, \phi)$ gives the directional characteristics of the antenna, i.e. it reflects that the farfield of a dipole is not uniform in space. The total electric field of an N-element antenna ensemble in the xy-plane (see Fig. 2b) is the sum of the electric fields of the individual antennas, with distance to the observation point r_n. In the far-field $1/r_n$ is approximated with $1/r$ and $exp(-ikr_n)$ with $exp(-ik(r - d_n cos(\xi_n)))$, where d_n is the Euclidian norm of the antenna-coordinates in the xy-plane, which is normal to the incident light. The electric field of multiple antennas, therefore, becomes

$$\mathbf{E} = i\eta kl \frac{e^{-ikr}}{4\pi r} \sum_{n=1}^{N} \mathbf{F_n}(\theta, \phi) e^{ikd_n cos(\xi_n)} I_n = i\eta kl \frac{e^{-ikr}}{4\pi r} \mathbf{G} \tag{2}$$

where $\mathbf{G}$ is the so-called array factor that determines the radiation pattern.[38] $cos(\xi_n) = cos(\theta)cos(\phi - \phi_n)$ and (d_n, ϕ_n) are the polar coordinates of a convenient reference point of the nth element. Since the scattered field strength is proportional to the incoming field along the long axis of the dipole, the excitation current for the nanorod antenna is given by

$$I_n = cos(\beta_n + \pi/4)cos(\psi) + sin(\beta_n + \pi/4)sin(\psi)e^{i\delta} \tag{3}$$

where ψ and δ describe the polarization of the incoming light using the Jones vector model of polarization in complex number representation.[39] β_n is the rotation of the nth dipole away from the x axis in the xy-plane. The excitation current of a cylindrical nanoantenna is rotationally invariant $(I_n = cos(\psi) + sin(\psi)e^{i\delta})$ and $I_n^2 = 1$. The angular-dependent vector is equal to[40]

$$\mathbf{F}(\theta, \phi) = sin(\phi - \beta_n)\hat{\boldsymbol{\phi}} - cos(\phi - \beta_n)sin(\theta)\hat{\boldsymbol{\theta}} \tag{4}$$

where $\hat{\boldsymbol{\phi}}$ and $\hat{\boldsymbol{\theta}}$ are azimuthal and polar unit vectors.

Speckle patterns obtained using equations (2)–(4) and the specific dimensions of the optical setup are compared with experimentally acquired images of scattered light in Fig. 3. The distance between fiber and metasurface is varied to change the number of nanoantennas

illuminated by the light source to change the speckle size. It is seen that the simulated speckle size matches the experimental speckle size resonably well. A line of bright speckles in the middle of the simulated image from left to right, most clearly discerned in Fig. 3a, is a result of the unit cell constraint, which adds a periodicity to the pattern. These pseudo-grating orders are absent in the experimental speckle patterns due to antenna interactions.
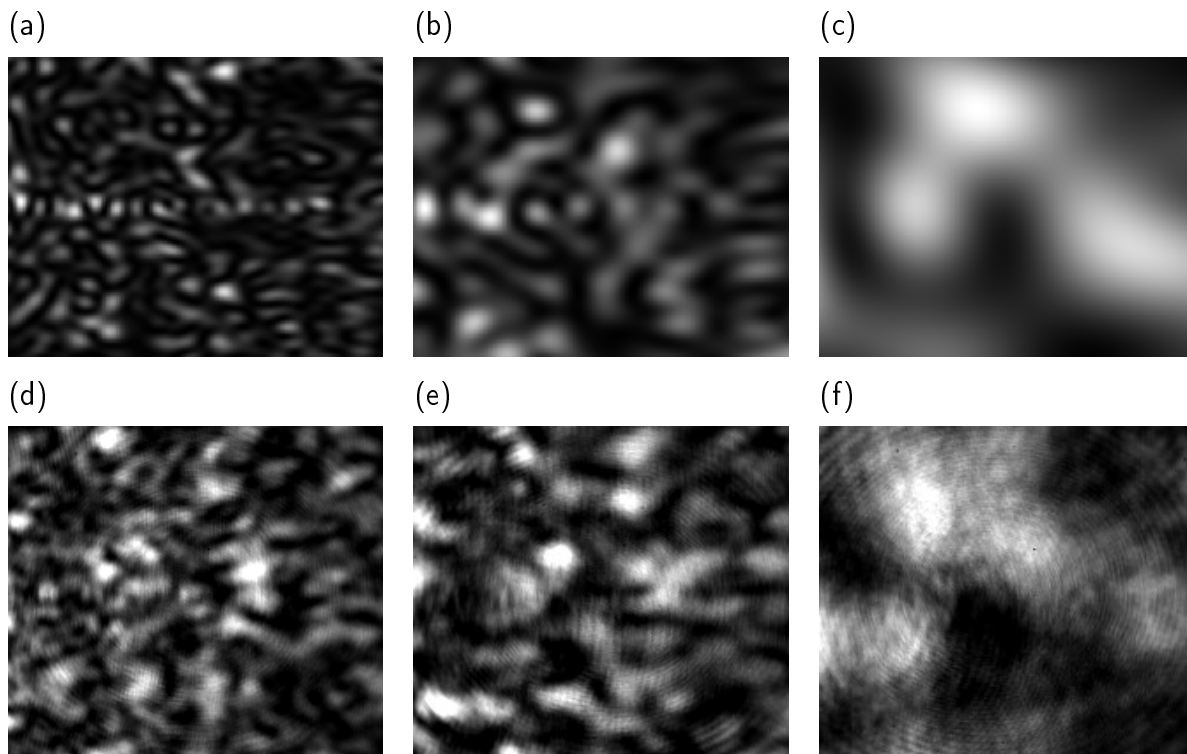

Figure 3: Simulated and experimental speckle images. (a)–(c) Simulated speckle images of (a) a 100×100 µm random gold nanorod pattern, (b) a 50×50 µm random gold nanorod pattern, and (c) a 12×12 µm random gold nanorod pattern. (d)–(f) Images of scattered light from random gold nanorod pattern recorded by an infrared camera. Distances between fiber and metasurface are (d) 500 µm, (e) 300 µm, (f) 30 µm.

Neural Network Architectures

It has been shown that deep neural networks can be used to take advantage of the inherent wavelength sensitivity of a metasurface polarimeter by producing a calibration that allows for measurement of the Stokes vector in a wide wavelength range without prior knowledge of the wavelength.[41] A polarimeter based on disordered photonic structures is not only very

sensitive to wavelength changes but also to mechanical vibrations and displacements. A deep neural network calibration that incorporates these mechanical variations in the learning process would therefore be expected to increase the stability of the polarimeter considerably. In this work, we explored two different network architectures: the multilayer perceptron (MLP), which accepts vectors as input and is one of the simplest neural network architectures and the convolutional neural network (CNN), which accepts tensors as inputs. The MLP model treats each input feature on exactly the same footing whereas the CNN model incorporates 2-dimensional information in the learning process by using a convolution operation.[42] The two neural network architectures are illustrated in Fig. 4. At a particular input wavelength, the relationship between the Stokes vector and the output (the scattered light intensities) can be well approximated by a linear transformation. We therefore considered the accuracy of the polarization measurement obtained using a linear regression model (LRM) for a given wavelength and position of light input to represent a benchmark of the irreducible error of the polarimeter device at that wavelength. A description of hyperparameters and training of the neural networks are found in the supplementary material.

Results

The speckle images recorded by the infrared camera contain 320×256 pixels and are downsampled using average pooling with a pool size of 16×16 before applying the MLP and LRM models in order to minimize redundant information by roughly matching the pixel size with the speckle size. Each speckle is an independent polarization analyzer depending on position and orientation of the nanoantennas and interference of the polarization components of the scattered light as described by the analytical model. After downsampling, the number of features or analyzer vectors in $\mathbf{A}$ is therefore 320, plotted in Fig. 5 for three nanorod structures with varying orientational constraints, measured at a wavelength of 1550 nm. The figure shows the normalized analyzer vectors of the three nanostructures plotted on a Poincaré
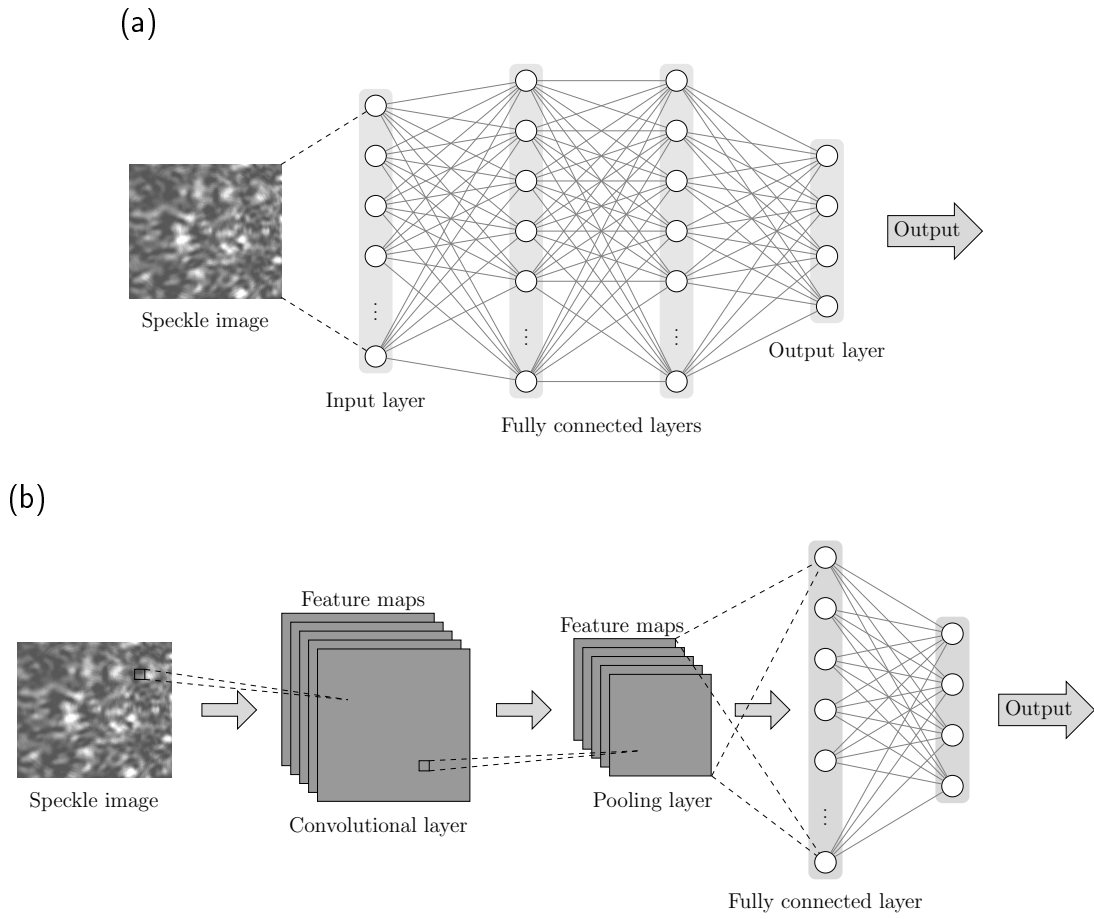
11

Figure 4: Schematics of the two neural network types: (a) the multilayer perceptron (MLP) and (b) the convolutional neural network (CNN). The MLP consists of fully connected layers: an input, an output, and one or more hidden layers. Every node in the hidden layer is activated by a nonlinear activation function after receiving input features that are multiplied with weigths and added a bias. The CNN adds two more types of layers: the convolutional layer that creates feature maps by convolving a filter around the input image and pooling layer that downsamples the input maps by applying an average or max filter to non-overlapping regions of the input maps.

sphere. The analyzer vectors of the metasurface with random antenna orientation and position are distributed randomly across the entire sphere thus forming a good basis for Stokes space, whereas the analyzer vectors accumulate increasingly around the negative S_1 axis (vertical linear polarization) as the orientational restriction on the nanorods is increased. The randomly oriented nanorod antennas each select for a specific linear polarization and the quasi-random antenna positions result in random phase shifts between interfering scattering fields that gives the analyzer vectors a random ellipticity. If all antennas are arranged vertically, then they only analyze one polarization (vertical linear polarization). The scattered light from all antennas will be of same polarization in a given direction and interference will therefore not change the ellipticity. Theoretically, the antenna design restricted to vertical orientations will not be able to function as a polarimeter, but antenna interactions will create sufficient variation of the analyzer vectors for the device to perform (low quality) polarization measurements. The validity of these arguments are supported by using the anytical model to extract the analyzer vectors. Complementary plots to Fig. 5a-c using the analytical model are found in the supplementary material. The intensity of scattered light from circular nanodisk antennas is not polarization-dependent. The nanodisk design therefore rely on antenna interactions.[43] Elliptical nanodisk will experience reduced antenna interaction especially along the semi-minor axis (b) and will behave more like the vertically oriented nanorod design as b is decreased. The effect of antenna design on the polarimeter performance is shown in Fig. 5d. Each of the designs are measured with 12,000 datapoints of random polarization states across a wavelength range of 1540–1560 nm in steps of 0.2 nm and a laser power varied between 1.5 and 3.0 mW. The difference between polarization measurements using the MLP model and reference polarizations is shown as angular error on the Poincaré sphere. The angular error decreases as the analyzer vector position becomes more evenly distributed over the Poincaré sphere. The measurements show that with a sufficient number of analyzers, disorder is not undesirable, it is instrumental in obtaining high quality polarization measurements.
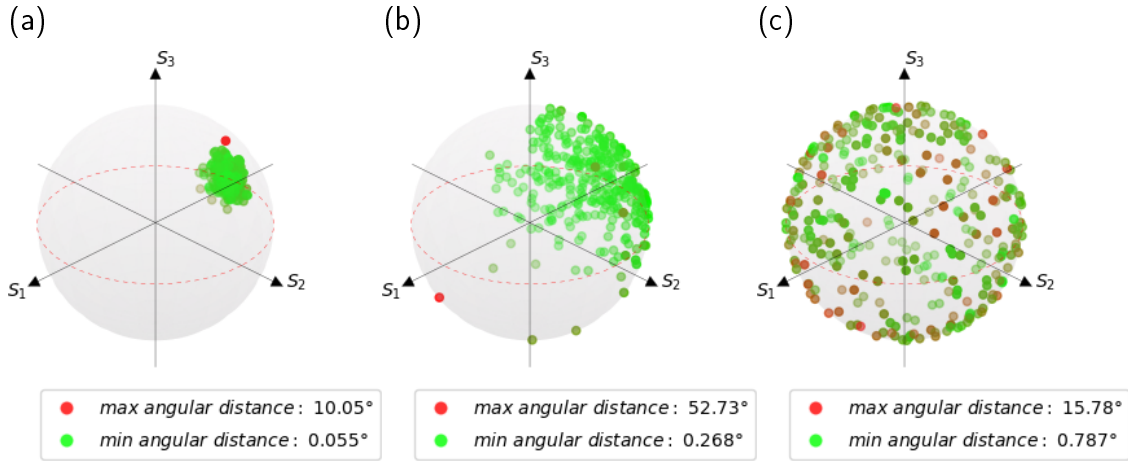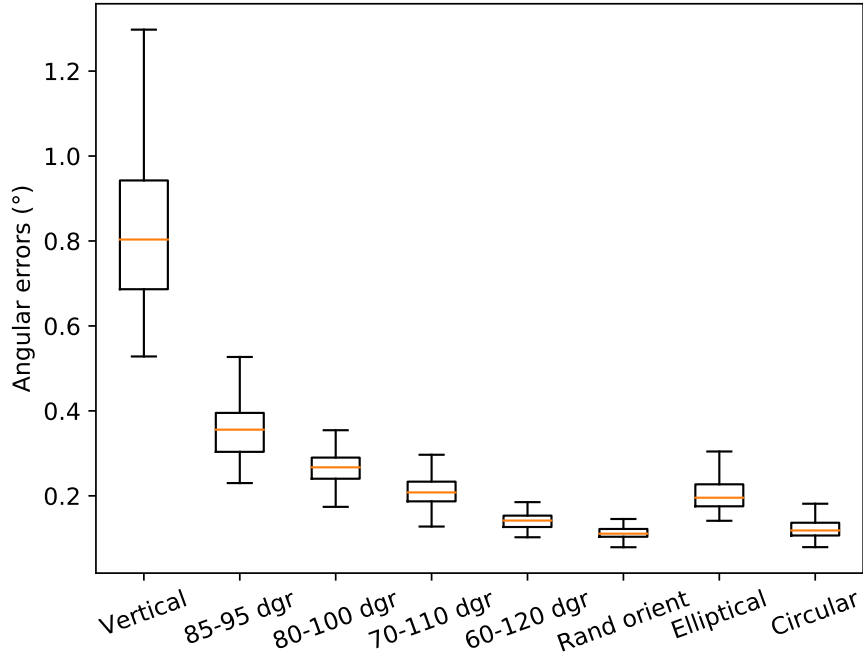
Figure 5: (a)–(c) Analyzer vector positions on a Poincaré sphere for three metasurface designs (360° views of the plots are found in supplementary material). The color of the dots illustrates the angular distance to the nearest analyzer vector from green (minimum distance) to red (maximum distance). Each design contains gold nanorods with quasi-random position in a unit cell and random orientation in a range of angles: (a) 85°–95°, (b) 60°–120° and (c) 0°–180° (no constraints on angular orientation). (d) Tukey boxplots showing the angular error between measured polarization states and reference polarizations measured by a commercial polarimeter. The first 6 boxes plot the data from nanorod design with decreasing constraints on the nanorod orientation. The last two boxes to the right plot data belonging to the nanodisk antenna designs with elliptical shape, where the semi-minor axis is half the length of the semi-major axis, and circular shape (Fig. 1d).

Fig. 6a compares the angular error of the three calibration methods (LRM, MLP, and CNN). The figure shows the angular error for a polarimeter based on the metasurface with randomly placed and oriented gold nanorods (Fig. 1c). The data set consists of 21,000 measurements distributed across the full C-band (1530–1565 nm) in steps of 0.2 nm. The laser power was varied between 1.5 and 3.0 mW. The CNN performs better than the MLP, since it is able to extract the 2-dimensional information contained in the speckle images. Furthermore, it performs just as well as the linear model. When a neural network calibration is used the polarization can therefore be measured without prior knowledge of the wavelength (inside the calibrated wavelength range) with the same accuracy as can be obtained with a calibration using the linear model where exact knowledge of the wavelength is required. The performance of the polarimeter is comparable to the accuracy of a commercial polarimeter as illustrated with a dashed line.

The performance of the polarimeter based on disordered photonic structures is sensitive to positional displacements. It was therefore sought to include eventual displacements in the learning model. This was realized by deliberately changing the position of the light source (the fiber tip) relative to the analyzer before each measurement to a random xyz coordinate within a $20{\times}20{\times}20$ µm grid using a piezoelectric motorized xyz stage. The measurements were made at a frequency of about $0.15\,\mathrm{s}^{-1}$ and are considered quasi-static with respect to time. Vibrational oscillations of different frequency are not included in the training data. The angular errors for these measurements are shown in Fig. 6b. With a mean angular error of 0.77° using MLP and 0.53° with CNN the neural network calibration results in a considerably lower error than the linear model (3.8°). The incorporation of wavelength and positional variations in the neural network models allows us to simultaneously measure the input wavelength and light source position, see Fig. S1 in the supplementary material.

It should be emphasized that the disordered polarization analyzer is well approximated by a linear model when wavelength and position is fixed (see Fig. 6a, LRM boxplot). The polarimeter is therefore no different than a conventional polarimeter such as the rotating-
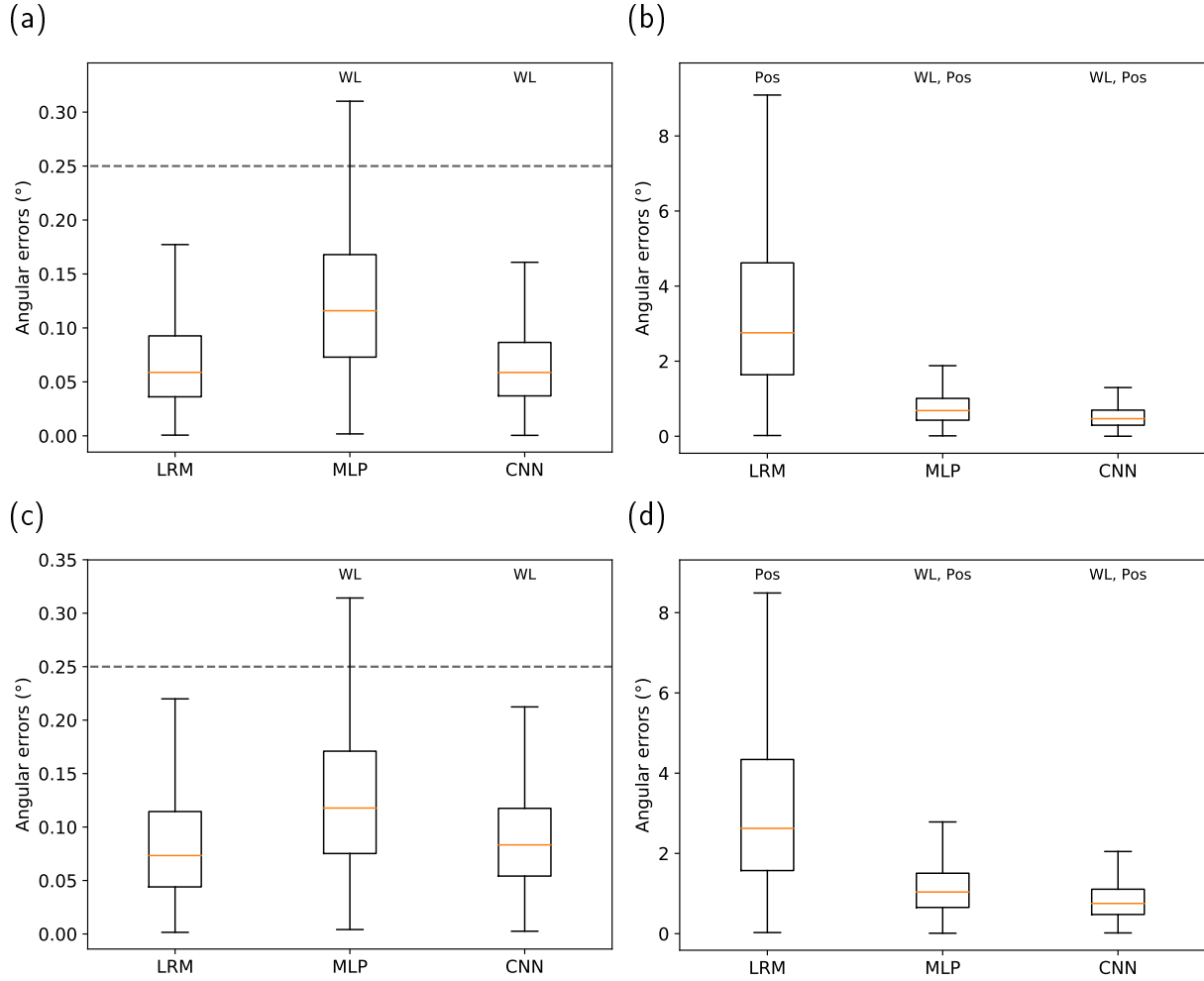
Figure 6: (a) Angular error of polarimeter based on gold nanorods using three calibration methods: linear regression model (LRM) with as many calibrations as measured wavelengths, multilayer perceptron neural network model (MLP), and convolutional neural network model (CNN). The position of the light source (cleaved single-mode fiber) is fixed. The dashed horizontal line indicates the angular error specification of a commercial fiber polarimeter (Thorlabs IPM5300). (b) Angular error for a nanorod antenna design using three calibration methods: LRM, MLP, and CNN, when (in addition to wavelength) the position of the light source is varied within a $20{\times}20{\times}20\,\mu m$ grid. (c)–(d) Angular error for a cellophane based polarimeter using three calibration methods: LRM, MLP, and CNN when position of the light source is (c) fixed and (d) varied within a $20{\times}20{\times}20\,\mu m$ grid. Above each boxplot is shown the varied parameters (except from polarization) that are unknown to the relevant model.

16

waveplate polarimeter. Machine learning methods are introduced only to alleviate the sensitivities of the linear model to small changes in wavelength and position. Deep learning methods are very powerful tools for solving complex problems, but it is very difficult to extract how they arrive at the solution. However, it is clear that the more sensitive the analyzer is to a varied parameter, the higher accuracy the model can obtain. Since the speckle pattern changes at a higher rate with wavelength than position the neural network models are therefore more efficient in predicting the wavelength parameter, see also supplementary material.

The measurements show that the neural network calibration improves the tolerance to mechanical instabilities of the polarimeter and suggest that accurate and robust polarimeters can be fabricated at extremely low cost using random metasurfaces. A fabrication procedure for a polarization analyzer based on disordered metallic nanoantennas could therefore consist simply of drying a drop of nanoparticles in colloidal suspension on a transparent surface[44] to replace high cost, low volume approaches such as electron-beam lithography. To emphasize this argument, we have replaced the random metasurface analyzer with a simple cellophane film. The results, plotted in Fig. 6c–d, show that the performance of the cellophane based polarimeter is comparable to the polarimeter based on metal nanoantennas. Cellophane is a birefringent material made of long, parallel strings of regenerated cellulose fibers arranged in a pseudo-grating.[45] The general shape of the scattered speckle pattern from the cellophane film is similar to the random metasurface speckle pattern. The light transmitted through the random metasurface is unscattered and therefore preserves its polarization whereas the cellophane is birefringent and therefore modifies the transmitted polarization. The cellophane film used in the experiment thus behaves like an imperfect quarter-wave plate. The cellophane-film polarimeter demonstrates that high quality polarimetric measurement can be achieved with extreme low-cost materials.

Summary

In summary, we have demonstrated deep neural network enhanced polarimeters based on disordered photonics structures, challenging the prevailing concepts of high-precision engineered polarization analyzers. The presented technology has the potential to provide a new class of extreme low-cost polarimeters and opens new avenues for the design of optical devices.

Acknowledgement

Supporting Information

Figs. S1 to S3, Prediction of wavelength and position, analytical analyzer vectors, sample preparation and deep learning models (PDF). Videos S1 to S3: 360° views of Figs. 5a-c.

Author Information

Corresponding Author

*E-mail: michaeljuhl@nmi.is

ORCID

Michael Juhl: 0000-0003-2142-7831

Kristjan Leosson: 0000-0002-7897-5911

Notes

The authors declare no competing financial interest.

References

(1) Azzam, R. M. A. Stokes-vector and Mueller-matrix polarimetry [Invited]. *J. Opt. Soc. Am. A* **2016**, *33*, 1396–1408.

(2) Azzam, R. M. A. The intertwined history of polarimetry and ellipsometry. *Thin Solid Films* **2011**, *519*, 2584–2588.

(3) Tyo, J. S.; Goldstein, D. L.; Chenault, D. B.; Shaw, J. A. Review of passive imaging polarimetry for remote sensing applications. *Appl. Opt.* **2006**, *45*, 5453–5469.

(4) Ghosh, N.; Vitkin, A. I. Tissue polarimetry: concepts, challenges, applications, and outlook. *J. Biomed. Opt.* **2011**, *16*, 110801.

(5) Westbrook, P. S.; Strasser, T. A.; Erdogan, T. In-line polarimeter using blazed fiber gratings. *IEEE Photon. Technol. Lett.* **2000**, *12*, 1352–1354.

(6) Peinado, A.; Lizana, A.; Vidal, J.; Iemmi, C.; Campos, J. Optimization and performance criteria of a Stokes polarimeter based on two variable retarders. *Opt. Express* **2010**, *18*, 9815–9830.

(7) Martínez-Ponce, G.; Solano, C.; Pérez-Barrios, C. Hybrid complete Mueller polarimeter based on phase modulators. *Opt. Lasers Eng.* **2011**, *49*, 723–728.

(8) Martínez, A. Polarimetry enabled by nanophotonics. *Science* **2018**, *362*, 750–751.

(9) Rubin, N. A.; D'Aversa, G.; Chevalier, P.; Shi, Z.; Chen, W. T.; Capasso, F. Matrix Fourier optics enables a compact full-Stokes polarization camera. *Science* **2019**, *365*.

(10) Rubin, N.; Zaidi, A.; Juhl, M.; Li, R.; Mueller, J. P. B.; Devlin, R.; Leosson, K.; Capasso, F. Polarization state generation and measurement with a single metasurface. *Opt. Express* **2018**, *26*, 21455–21478.

(11) Juhl, M.; Mueller, J. P. B.; Leosson, K. Metasurface polarimeter on optical fiber facet by nano-transfer to UV-curable hybrid polymer. *IEEE J. Sel. Top. Quantum Electron.* **2019**, *25*, 1–7.

(12) Chen, Y.; Ding, F.; Coello, V.; Bozhevolnyi, S. I. On-chip spectropolarimetry by finger-printing with random surface arrays of nanoparticles. *ACS Photon.* **2017**, *5*, 1703–1710.

(13) Capasso, F. The future and promise of flat optics: a personal perspective. *Nanophotonics* **2018**, *7*, 953–957.

(14) Pors, A.; Nielsen, M. G.; Bozhevolnyi, S. I. Plasmonic metagratings for simultaneous determination of Stokes parameters. *Optica* **2015**, *2*, 716–723.

(15) Arbabi, E.; Kamali, S. M.; Arbabi, A.; Faraon, A. Full-Stokes imaging polarimetry using dielectric metasurfaces. *ACS Photon.* **2018**, *5*, 3132–3140.

(16) Mueller, J. P. B.; Leosson, K.; Capasso, F. Ultracompact metasurface in-line polarimeter. *Optica* **2016**, *3*, 42–47.

(17) Wiersma, D. S. Disordered photonics. *Nat. Photon.* **2013**, *7*, 188.

(18) Beenakker, C. W. Random-matrix theory of quantum transport. *Rev. Mod. Phys.* **1997**, *69*, 731.

(19) Mosk, A. P.; Lagendijk, A.; Lerosey, G.; Fink, M. Controlling waves in space and time for imaging and focusing in complex media. *Nat. Photon.* **2012**, *6*, 283.

(20) Li, Y.; Xue, Y.; Tian, L. Deep speckle correlation: a deep learning approach toward scalable imaging through scattering media. *Optica* **2018**, *5*, 1181–1190.

(21) Jang, M.; Horie, Y.; Shibukawa, A.; Brake, J.; Liu, Y.; Kamali, S. M.; Arbabi, A.; Ruan, H.; Faraon, A.; Yang, C. Wavefront shaping with disorder-engineered metasurfaces. *Nat. Photon.* **2018**, *12*, 84.

(22) Park, J.-H.; Park, C.; Yu, H.; Park, J.; Han, S.; Shin, J.; Ko, S. H.; Nam, K. T.; Cho, Y.-H.; Park, Y. Subwavelength light focusing using random nanoparticles. *Nat. Photon.* **2013**, *7*, 454.

(23) Kelzenberg, M. D.; Boettcher, S. W.; Petykiewicz, J. A.; Turner-Evans, D. B.; Putnam, M. C.; Warren, E. L.; Spurgeon, J. M.; Briggs, R. M.; Lewis, N. S.; Atwater, H. A. Enhanced absorption and carrier collection in Si wire arrays for photovoltaic applications. *Nat. Mater.* **2010**, *9*, 239.

(24) Wiersma, D. S. The physics and applications of random lasers. *Nat. Phys.* **2008**, *4*, 359.

(25) Cao, H.; Zhao, Y.; Ho, S.-T.; Seelig, E.; Wang, Q.; Chang, R. P. Random laser action in semiconductor powder. *Phys. Rev. Lett.* **1999**, *82*, 2278.

(26) Goodfellow, I.; Bengio, Y.; Courville, A. *Deep Learning*; The MIT Press: Cambridge MA, 2016.

(27) Borhani, N.; Kakkava, E.; Moser, C.; Psaltis, D. Learning to see through multimode fibers. *Optica* **2018**, *5*, 960–966.

(28) Ghosh, K.; Stuke, A.; Todorović, M.; Jørgensen, P. B.; Schmidt, M. N.; Vehtari, A.; Rinke, P. Deep learning spectroscopy: neural networks for molecular excitation spectra. *Adv. Sci.* **2019**, *6*, 1801367.

(29) Musumeci, F.; Rottondi, C.; Nag, A.; Macaluso, I.; Zibar, D.; Ruffini, M.; Tornatore, M. An overview on application of machine learning techniques in optical networks. *IEEE Commun. Surv. Tutor.* **2018**, *21*, 1383–1408.

(30) Hughes, T. W.; Minkov, M.; Shi, Y.; Fan, S. Training of photonic neural networks through in situ backpropagation and gradient measurement. *Optica* **2018**, *5*, 864–871.

(31) Berry, H. G.; Gabrielse, G.; Livingston, A. Measurement of the Stokes parameters of light. *Appl. Opt.* **1977**, *16*, 3200–3205.

(32) Azzam, R. M. A.; Elminyawi, I. M.; El-Saba, A. M. General analysis and optimization of the four-detector photopolarimeter. *J. Opt. Soc. Am. A* **1988**, *5*, 681–689.

(33) Boulbry, B.; Ramella-Roman, J. C.; Germer, T. A. Improved method for calibrating a Stokes polarimeter. *Appl. Opt.* **2007**, *46*, 8533–8541.

(34) Macias-Romero, C.; Török, P. Eigenvalue calibration methods for polarimetry. *J. Eur. Opt. Soc. Rapid* **2012**, *7*.

(35) Foreman, M. R.; Favaro, A.; Aiello, A. Optimal frames for polarization state reconstruction. *Phys. Rev. Lett.* **2015**, *115*, 263901.

(36) Juhl, M. Metasurface Polarimetry. Ph.D. thesis, University of Iceland, 2018.

(37) Biagioni, P.; Huang, J.-S.; Hecht, B. Nanoantennas for visible and infrared radiation. *Rep. Prog. Phys.* **2012**, *75*, 024402.

(38) Juhl, M.; Mendoza, C.; Mueller, J. P. B.; Capasso, F.; Leosson, K. Performance characteristics of 4-port in-plane and out-of-plane in-line metasurface polarimeters. *Opt. Express* **2017**, *25*, 28697–28709.

(39) Damask, J. N. *Polarization Optics in Telecommunication*; New York, Springer, 2005.

(40) Sahalos, J. N. *Orthogonal Methods for Array Synthesis: Theory and the ORAMA Computer Tool*; Chichester UK, John Wiley & Sons, Ltd, 2006.

(41) Magnusson, E. B.; Mueller, J. P. B.; Juhl, M.; Mendoza, C.; Leosson, K. Neural polarimeter and wavemeter. *ACS Photon.* **2018**, *5*, 2682–2687.

(42) LeCun, Y.; Bottou, L.; Bengio, Y.; Haffner, P., et al. Gradient-based learning applied to document recognition. *Proc. IEEE* **1998**, *86*, 2278–2324.

(43) Rechberger, W.; Hohenau, A.; Leitner, A.; Krenn, J.; Lamprecht, B.; Aussenegg, F. Optical properties of two interacting gold nanoparticles. *Opt. commun.* **2003**, *220*, 137–141.

(44) Yunker, P. J.; Still, T.; Lohr, M. A.; Yodh, A. Suppression of the coffee-ring effect by shape-dependent capillary interactions. *Nature* **2011**, *476*, 308.

(45) Lee, S.; Kim, J.-H.; Kang, K.; Kim, J.; Kim, H. S.; Yang, C. Characterization of micro-scale creep deformation of an electro-active paper actuator. *Smart Mater. Struct.* **2009**, *18*, 095008.

For Table of Contents Use Only

Polarimetry with disordered photonic structures

Michael Juhl and Kristjan Leosson

Fabrication and characterization of deep neural network assisted polarimeters based on disordered photonic structures, demonstrating how disordered photonic structures fabricated without the use of any nanolithography techniques can enable accurate analysis of optical signals.